Optimizing Power Transfer Efficiency in Biomedical Implants: A Comparative Analysis of SS and SP Inductive Link Topologies

Fen Xia, *Student Member, IEEE*, Fangyu Mao, *Member, IEEE*, Yan Lu, *Senior Member, IEEE*, and Mohamad Sawan, *Life Fellow, IEEE*

***Abstract*—Inductive link intended to deliver energy to implantable devices is recently becoming a popular method. To improve link efficiency, the compensated capacitors are adopted to resonate at the same frequency with the power transfer frequency on both sides. However, there is limited research on link efficiency and output power concerning quality factors, the selection between serial–parallel (SP) and serial–serial (SS) topologies, as well as coil design. This study delves into the efficiency of SP and SS topologies using rigorous mathematical derivations with reflected impedance models in terms of quality factors. It introduces a selection factor to help choose topology based on link efficiency. Results show that SS is better when the load quality factor (Q_L) is lower than the selection factor, and vice versa. The study also examines the performance limits of both topologies concerning frequency, inductance, and load impedance. It proposes a specific Q_L for maximum efficiency and a coil design procedure considering specific absorption rate limitations. By leveraging simulations and the design procedure, the study manufactures a pair of flexible coils for biomedical use. The designed link achieves a 62.99% efficiency under a 500 Ω load, with an overall efficiency of 46.96% including a passive rectifier.**

***Index Terms*—Biomedical, coil design, compensated topology, implant, inductive link, link efficiency, specific absorption rate (SAR), selection factor.**

I. Introduction

WIRELESS power transfer (WPT), based on inductive links, has gained popularity with advancements in modern power electronics, attributed to key advantages including the absence of exposed electrical contacts, heightened reliability, and high levels of link efficiency (η_{Link}) [1]. WPT-based biomedical implants, such as cardiac pacemakers [2], retinal prostheses [3], and hypoglossal nerve stimulators [4], must prioritize considerations to achieve low-power consumption, minimal footprint, and optimal power conversion efficiency. Fig. 1 illustrates a simplified architecture of a typical inductive coupling implantable system, including dual coupled coils, a power management module (PMM), and a load. PMM can be integrated on a chip to minimize invasive areas. An inductive link exhibits higher η_{Link} with a larger coil size, yet it occupies a larger area. Achieving both high η_{Link} and a minimally invasive area in the design of an inductive link poses a significant challenge.

The compensation method can enhance η_{Link} by mitigating the reactance of the primary input impedance [10]. Link efficiency is intricately related to the type of compensation topology, the size of the receiver coil, operation frequency, and load impedance [11], [12]. However, there is a wide range of variations of these factors. As indicated in Table I, η_{Link}

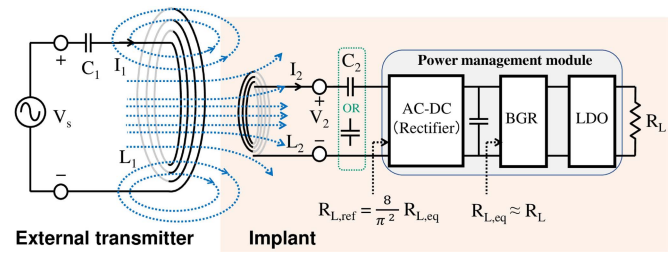

Fig. 1. Architecture of a typical inductive coupling implantable biomedical system featuring coupled coils, a PMM, and a load.

TABLE I
Various Parameters of an Inductive Link Applied in Implant

Ref.	[4]	[5]	[6]	[7]	[8]	[9]
DRx. (mm)	9.2	26	0.5	4.7	N/A	40
L_2 (μH)	0.5	0.475	N/A	0.044	0.5	1.05
R_L ($k\Omega$)	1	0.51	N/A	N/A	10	N/A
Freq. (MHz)	2	13.56	1000	400	13.56	6.78
Topology	SP	SP	SP	SP	SS	SS
η_{Link} (%)	39.8	N/A	0.16	0.12	66.5	90.3
DRx.: outer diameter or maximum side length of receiver.						

Manuscript received 15 December 2023; revised 20 February 2024 and 20 April 2024; accepted 13 May 2024. Date of publication 17 May 2024; date of current version 16 July 2024. This work was supported in part by the Westlake University under Grant 10318A992001, in part by the Zhejiang Leading Innovative and Entrepreneur Team Introduction Program under Grant 2020R01005, and in part by the Zhejiang Key R&D Program under Grant 2021C03002. Recommended for publication by Associate Editor M. Ponce-Silva. *(Corresponding author: Mohamad Sawan.)*

Fen Xia is with the CenBRAIN Neurotech Center of Excellence, School of Engineering, Westlake University, Hangzhou 310024, China, and also with the Zhejiang University, Hangzhou 310024, China (e-mail: xiafen@westlake.edu.cn).

Fangyu Mao is with the Light Semibucks (Wuxi) Company Limited, Shanghai 200131, China (e-mail: maofy@semibucks.com).

Yan Lu is with the Institute of Microelectronics, University of Macau, Macau 999078, China (e-mail: yanlu@um.edu.mo).

Mohamad Sawan is with the CenBRAIN Neurotech Center of Excellence, School of Engineering, Westlake University, Hangzhou 310024, China (e-mail: sawan@westlake.edu.cn).

Color versions of one or more figures in this article are available at https://doi.org/10.1109/TPEL.2024.3402238.

Digital Object Identifier 10.1109/TPEL.2024.3402238

© 2024 The Authors. This work is licensed under a Creative Commons Attribution 4.0 License. For more information, see https://creativecommons.org/licenses/by/4.0/

spans from 0.12% to 90.3%, with serial–parallel (SP) topology chosen in [4], [5], [6], and [7] and serial–serial (SS) topology selected in [8] and [9]. Besides, operating frequencies range from 2 [4] to 1000 MHz [6], conforming to industrial scientific and medical (ISM) standards [13]. Similar variability exists in the size of the receiver coil and the load impedance defined by the nerve–electrode interface (NEI). Crucially, carefully selecting an appropriate compensation topology is paramount, given its substantial influence on other factors related to link efficiency.

The selection between SS and SP structures was discussed in [14]; however, the study only focused on the frequency boundary. Ishihara et al.[15] introduced a quasi-duality strategy for analyzing SS and SP topologies. This study employed approximate equivalent circuit structures rather than exact representations, and solely discussed the load impedance boundary. The reflected impedance model is equivalent to the conventional transformer model in an inductive link. This model has been utilized for the analysis of SS and SP topologies in [16] and [17]. In [16], the η_{Link} formula was explicitly expressed with quality factors. However, it assumed a real reflected impedance from the primary coil, complicating η_{Link} calculations unnecessarily [17]. Notably, Lu and Ki [17] did not derive η_{Link} in terms of quality factors, and the selection analysis remains unexplored in both studies to date. Ibrahim and Kiani [18] investigated quality factors but was limited to SP topology. In addition, previous studies did not address the design of an inductive link for maximum efficiency at a specific load impedance or consider SAR limitations critical in biomedical applications.

In addition, optimizing coil design can significantly enhance η_{Link} by tuning parameters such as turns, wire-width, and trace-pitch [19], [20]. It improves the self-inductance and/or reduces the parasitic impedance of the coil, consequently enhancing the quality factor and η_{Link} [19]. While integrating resonant coils into three or four-coil systems boosts η_{Link} [21], [22], it increases invasiveness. A recent innovative approach, presented in [23], [24], and [25], focuses on enhancing the quality factor by introducing asymmetry in wire-width and trace-pitch within coil designs while maintaining a uniform outer radius. However, these studies were confined to single-layer coil design and did not consider factors, such as two-layer coil structure, load impedance, SAR limitations, and topology analysis between SS and SP.

The impedance control method enhances η_{Link} by optimizing load impedance at a specific value [26], [27], [28], facilitated by a circuit block positioned between the receiver coil and the load (R_L). In a WPT-based biomedical system, the impedance observed from the receiver coil ($R_{L,\text{ref}}$) closely matches R_L [29], as depicted in Fig. 1, obviating the need for this impedance controller. In strong coupling scenarios, where frequency splitting occurs, the frequency control technique stabilizes the voltage conversion ratio against load impedance variations [30], [31] by adjusting the operating frequency. Moreover, multiple harmonic analysis can be employed to evaluate the performance of WPT systems under conditions of strong coupling or heavy loads [32], [33], [34]. In contrast, biomedical implants utilize a weak coupling inductive link and operate under milliamp-level load currents [1], [33], effectively mitigating frequency splitting.

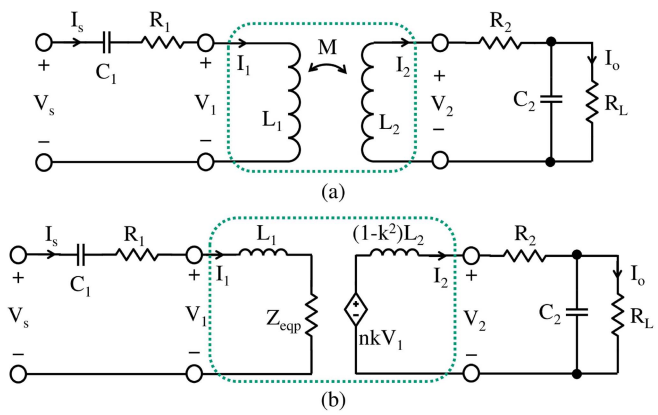

Fig. 2. (a) Circuit configuration of coupled coils arranged in a SP resonant topology with parasitic resistance. (b) Equivalent reflected impedance model.

As a result, the coupling mode theory with fundamental harmonic frequency analysis suffices for achieving precision [33], [34]. In biomedical applications, external and internal topologies resonate at the same frequency [4], [6], [7], [29] to maximize link efficiency ($\eta_{\max}$) by tuning the external capacitor [8]. In addition, the internal low dropout can deliver a constant voltage with considerable power conversion efficiency under maximum current load, rendering a frequency controller unnecessary in this study.

This article conducts an in-depth analysis of SS and SP topologies by evaluating η_{Link} and output power in terms of quality factors. It employs a reflected impedance model alongside fundamental frequency analysis (see Section II). The derived formulas for η_{Link} are then applied to two critical aspects (see Section III): SS versus SP topology selection, and the pursuit of $\eta_{\max}$. The analysis considers various factors, such as operating frequency, implantable coil inductance, and load impedance, providing insights into the boundary between SS and SP topologies and the conditions for achieving $\eta_{\max}$. Notably, the study provides a design procedure for an inductive link featuring a two-layer asymmetric receiver coil to achieve $\eta_{\max}$ at a predefined load impedance. Section IV validates the selection and boundary analyses through simulations, examining fluctuations in η_{Link} and output power under varying loads at 300 and 400 MHz frequencies. In addition, it presents the design and performance measurement of an inductive link operating at 13.56 MHz. Finally, Section V concludes this article.

II. Resonant Inductive Link

As the derivation of η_{Link} and output power of SS topology is much easier than that of SP topology, this article omits the comprehensive procedure for SS.

A. SP Topology

The circuit structure of the SP resonant inductive link is shown in Fig. 2. L_1 and L_2 denote the primary inductance and secondary inductance, respectively, M is the mutual inductance, R_1 and R_2 refer to the parasitic resistances of the primary and

secondary coils, respectively, and R_L signifies the load. When analyzing η_{Link} and output power for SS and SP topologies, the capacitance values of the compensation capacitors (C_1 and C_2) are defined to make sure that both sides are resonant at the same frequency with the power transfer frequency f_0, as follows:

$$f_0 = \frac{1}{2\pi\sqrt{L_1C_1}} = \frac{1}{2\pi\sqrt{L_2C_2}} = \frac{\omega_0}{2\pi}. \tag{1}$$

The quality factors are defined as

$$Q_1 = \frac{\omega L_1}{R_1}, Q_2 = \frac{\omega L_2}{R_2}, Q_L = \frac{R_L}{\omega L_2} \tag{2}$$

and the coupling coefficient k and turns ratio n are given

$$k = \frac{M}{\sqrt{L_1L_2}}, n = \sqrt{\frac{L_2}{L_1}}. \tag{3}$$

The analysis of η_{Link} and output power involves the following six steps.

1) *Formulate the equations of V_s and V_2 in Fig. 2(a):*

$$V_s = \left(\frac{1}{j\omega C_1} + R_1 + j\omega L_1\right) I_1 - j\omega M I_2 \tag{4a}$$

$$V_2 = j\omega M I_1 - j\omega L_2 I_2 = \left(R_2 + \frac{1}{j\omega C_2} \,||\, R_L\right) I_2. \tag{4b}$$

2) *Derive the expression for I_2 in terms of I_1 in SP topology:* The total impedance of the secondary side is named as Z_{2p}. with the same resonance frequency provided in (1), Z_{2p} can be expressed in the form of quality factors as

$$\begin{aligned} Z_{2p} &= j\omega L_2 + R_2 + \frac{1}{j\omega C_2} \,||\, R_L \\ &= R_2\left(1 + \frac{Q_2Q_L}{1+Q_L^2} + jQ_2\frac{1}{1+Q_L^2}\right). \end{aligned} \tag{5}$$

From (4b), I_2 can be deduced as

$$I_2 = \frac{j\omega M}{j\omega L_2 + R_2 + \frac{1}{j\omega C_2} \,||\, R_L} I_1 = \frac{j\omega M}{Z_{2p}} I_1. \tag{6}$$

3) *Determine the reflected impedance:* Substitute I_2 in (4a) with the expression from (6), the reflected impedance Z_{eqp} can be derived as

$$Z_{\text{eqp}} = \frac{\omega_0^2 M^2}{Z_{2p}}. \tag{7}$$

4) *Compute the input current I_1 as a function of I_o:* Notably, the current I_o that flows through the load is different from I_2. Then, the input current I_1 can be derived based on (6) as

$$\begin{aligned} I_1 &= \frac{Z_{2p}}{j\omega M} I_2 = \frac{Z_{2p}}{j\omega M}(1 + jQ_L) I_o \\ &= \frac{R_2\left(1 + \frac{Q_2Q_L}{1+Q_L^2} + j\frac{Q_2}{1+Q_L^2}\right)}{j\omega M}(1 + jQ_L) I_o. \end{aligned} \tag{8}$$

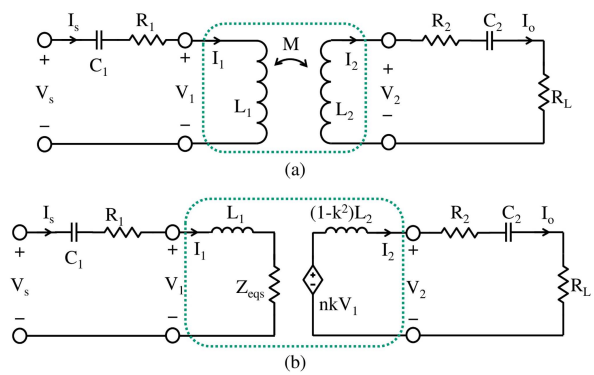

Fig. 3. (a) Circuit configuration of coupled coils arranged in a series-serial resonant topology with parasitic resistance. (b) Equivalent reflected impedance model.

5) *Derive η_{Link} in terms of quality factors:* Link efficiency is defined as

$$\eta_{\text{Link}} = \frac{P_{\text{out}}}{Re\,(P_{in})} = \frac{\frac{1}{2}R_L I_o^2}{\frac{1}{2}Re\,(Z_{1p})\, I_1 I_1^*} \tag{9}$$

where P_{in} is the input power [35] given by $P_{\text{in}} = \frac{1}{2}V_s I_1^*$, and Z_{1p} is the total impedance of the primary side, which is a complex number, as given by

$$\begin{aligned} Z_{1p} &= R_1 + \frac{(\omega M)^2}{Z_{2p}} = R_1\left[1 + \frac{(\omega M)^2}{R_1 Z_{2p}}\right] \\ &= \frac{R_L}{n^2 Q_1 Q_L}\left(1 + \frac{k^2 Q_1 Q_2}{1 + \frac{Q_2Q_L}{1+Q_L^2} + j\frac{Q_2}{1+Q_L^2}}\right). \end{aligned} \tag{10}$$

By deriving the real part of Z_{1p} from the equation given in (10), the η_{Link} for SP topology can be determined concerning the quality factors

$$\eta_{\text{SP}} = \frac{\frac{1}{(1+Q_L^2)} k^2 Q_1 Q_2^2 Q_L}{\left(1 + \frac{Q_2Q_L}{1+Q_L^2}\right)^2 + \left(\frac{Q_2}{1+Q_L^2}\right)^2 + k^2 Q_1 Q_2\left(1 + \frac{Q_2Q_L}{1+Q_L^2}\right)}. \tag{11}$$

6) *Calculate the output power in terms of input current I_1:* Based on (8), P_o can be calculated related to I_1 as

$$\begin{aligned} P_o &= \frac{1}{2} I_o I_o^* R_L \\ &= \frac{k^2 Q_2^2}{2n^2(1+Q_L^2)\left[\left(1 + \frac{Q_2Q_L}{1+Q_L^2}\right)^2 + \frac{Q_2^2}{(1+Q_L^2)^2}\right]} I_1^2 R_L. \end{aligned} \tag{12}$$

B. SS Topology

Fig. 3 depicts the circuit of SS resonant topology and the corresponding reflected impedance model. The reflected (or equivalent) impedance Z_{eqs} in the primary side is derived as

$$Z_{\text{eqs}} = \frac{\omega_0^2 M^2}{R_2 + R_L}. \tag{13}$$

In SS resonant topology, the η_{Link} is derived as follows:

$$\eta_{\text{SS}} = \frac{1}{1 + \frac{1}{Q_2 Q_L} + \frac{1}{k^2}\frac{1}{Q_1 Q_L}\left(\frac{1}{Q_2} + Q_L\right)^2}. \tag{14}$$

The output power P_o can be calculated related to I_1 as

$$P_o = \frac{1}{2} I_2 I_2^* R_L = \frac{k^2}{2n^2}\left(\frac{Q_2}{1 + Q_2 Q_L}\right)^2 I_1^2 R_L. \tag{15}$$

III. Application-Oriented Analysis

A selection factor based on quality factors is introduced to guide the choice between SS and SP topologies in terms of LE. Notably, the article explores the optimal load quality factor that results in $\eta_{\max}$. Considering SAR limitations in biomedical applications, a design procedure is proposed to achieve $\eta_{\max}$.

A. Proposed Selection Factor

The η_{Link} equations for SS and SP topologies are articulated in terms of the quality factors, as denoted by (14) for SS and (11) for SP. Since Q_1 and Q_2 are determined by the structure of both coils, the analysis of Q_L is essential under the condition of a specified inductive link.

The boundary to choose SS and SP should be calculated by making (11) equals (14). By solving this equation, Q_L can be derived as

$$Q_{\text{Lsf}} = \frac{Q_2}{\sqrt{Q_2^2 - 1 - k^2 Q_1 Q_2}} \tag{16}$$

where Q_{Lsf} is denoted as the selection factor. Then verify that there is only one point of intersection of SS and SP topologies. By setting the derivative of η_{Link} expressed in (14) for Q_L to zero, $\eta_{\max}$ for SS topology can be ascertained. This optimum value is achieved when Q_L equals

$$Q_{Ls} = \sqrt{\frac{1 + k^2 Q_1 Q_2}{Q_2^2}}. \tag{17}$$

Considering

$$\frac{k^2 Q_1}{Q_2} = \frac{M^2}{L_1 L_2} \cdot \frac{\omega L_1 R_2}{\omega L_2 R_1} = \frac{M^2}{L_2^2}\frac{R_2}{R_1} \tag{18}$$

it is evident that M^2/L_2^2 is significantly less than 1, and R_2/R_1 is smaller than 1 as well. In addition, Q_2 notably exceeds 1. Consequently, it is reasonable to derive that the quality factor Q_{ls} is markedly smaller than 1. Furthermore, the analysis indicates that the selection factor in (16) is negligibly higher than 1.

When Q_L is less than Q_{ls}, the slope factor of the denominator in (14) concerning Q_L is negative. This signifies that as Q_L increases, the denominator decreases, increasing η_{Link}. Conversely, when Q_L exceeds Q_{ls}, the slope factor of the denominator in (14) is positive. In this scenario, the denominator increases as Q_L increases, leading to a decrease in η_{Link} as Q_L increases.

Meanwhile, the $\eta_{\max}$ for SP topology can be determined, by setting the differentiation of η_{Link} for Q_L to zero. This occurs when Q_L is equal to

$$Q_{\text{Lp}} = \sqrt{1 + \frac{Q_2^2}{1 + k^2 Q_1 Q_2}}. \tag{19}$$

Since the value of (17) is less than 1, it is easy to deduce that the value of (19) exceeds 1, and the selection factor outlined in (16) hovers around 1. This phenomenon plays a crucial role in determining the singular point where the η_{Link} of both SS and SP topologies intersect uniquely.

TABLE II
Selection Between SS and SP Topologies

Load quality factor Q_L	Link efficiency
$Q_L < Q_{Lsf}$	SS topology > SP topology
$Q_L = Q_{Lsf}$	SS topology = SP topology
$Q_L > Q_{Lsf}$	SS topology < SP topology

The selection between SS and SP topologies is summarized in Table II. When the value of load quality factor ($Q_L = R_L/\omega L_2$) is lower than the selection factor Q_{Lsf} specified in (16), SS demonstrates superior performance compared to SP, and the η_{Link} for SS topology is computed using (14). Conversely, if the value of Q_L exceeds the value of Q_{Lsf}, SP exhibits better performance than SS, and the η_{Link} for this topology is determined using (11).

B. Analysis on Load Quality Factor

1) $Q_L = 1$ ($Q_L \lesssim Q_{Lsf}$):

The η_{Link} for SS topology, expressed in (14), can be formulated as follows:

$$\eta_{\text{SS}}|_{Q_L=1} = \frac{1}{1 + \frac{1}{Q_2} + \frac{1}{k^2}\frac{1}{Q_1}\left(\frac{1}{Q_2} + 1\right)^2}. \tag{20}$$

The η_{Link} for SP topology, as given in (11), can be expressed as follows:

$$\begin{aligned}\eta_{\text{SP}}|_{Q_L=1} &= \frac{\frac{1}{2}k^2 Q_1 Q_2^2}{\left(1 + \frac{Q_2}{2}\right)^2 + \left(\frac{Q_2}{2}\right)^2 + k^2 Q_1 Q_2\left(1 + \frac{Q_2}{2}\right)} \\ &= \frac{1}{1 + \frac{1}{Q_2} + \frac{1}{k^2}\frac{1}{Q_1}\left[\left(\frac{1}{Q_2} + 1\right)^2 + 2 + \frac{1}{Q_2^2}\right]}.\end{aligned} \tag{21}$$

SS topology shows a better performance in this condition.

2) $Q_L > 1$ ($Q_L > Q_{Lsf}$):

$$\eta_{SP,\max} = \frac{k^2 Q_1 Q_2}{k^2 Q_1 Q_2 + 2 + 2\sqrt{1 + k^2 Q_1 Q_2}\sqrt{1 + \frac{1 + k^2 Q_1 Q_2}{Q_2^2}}}. \tag{22}$$

When Q_L equals Q_{lp}, the η_{Link} in SP topology reaches its maximum value, as indicated by

$$\eta_{\text{SP,max}} = \frac{k^2 Q_1 Q_2}{k^2 Q_1 Q_2 + 2 + 2\sqrt{1 + k^2 Q_1 Q_2}\sqrt{1 + \frac{1 + k^2 Q_1 Q_2}{Q_2^2}}}. \tag{23}$$

When $Q_L \gg 1$ ($Q_L \gg Q_{\text{Lsf}}$), η_{Link} in (11) can be simplified as

$$\eta_{\text{SP}} \approx \frac{\frac{1}{Q_L^2} k^2 Q_1 Q_2^2 Q_L}{\left(1+\frac{Q_2}{Q_L}\right)^2 + \left(\frac{Q_2}{Q_L^2}\right)^2 + k^2 Q_1 Q_2 \left(1+\frac{Q_2}{Q_L}\right)}. \tag{24}$$

As $Q_2/Q_L \gg Q_2/Q_L^2$, Q_2/Q_L^2 can be neglected in the denominator term, then (24) can be further simplified as

$$\begin{aligned}\eta_{\text{SP}} &\approx \frac{\frac{1}{Q_L^2} k^2 Q_1 Q_2^2 Q_L}{\left(1+\frac{Q_2}{Q_L}\right)^2 + k^2 Q_1 Q_2 \left(1+\frac{Q_2}{Q_L}\right)} \\ &= \frac{k^2 Q_1/Q_L}{\left(\frac{1}{Q_2}+\frac{1}{Q_L}\right)^2 + k^2 Q_1 \left(\frac{1}{Q_2}+\frac{1}{Q_L}\right)} \\ &= \frac{k^2 Q_1 Q_{2L}}{1+k^2 Q_1 Q_{2L}} \frac{Q_{2L}}{Q_L}\end{aligned} \tag{25}$$

where $Q_{2L} = Q_2 Q_L/(Q_2+Q_L)$. This equation is the same as (4) provided in [18]. Under the condition of the extremely high value of Q_L, the impedance in the secondary side in SP resonant topology in (5) can be approximately expressed as

$$Z_{2p} \approx R_2 \left(1+\frac{Q_2}{Q_L}\right). \tag{26}$$

In the same resonant condition, the impedance in the secondary side in SS topology can be expressed as

$$Z_{2s} = R_2 \left(1+\frac{R_L}{R_2}\right) = R_2 \left(1+Q_2 Q_L\right). \tag{27}$$

Comparing (26) and (27), we can easily find that Z_{2s} is much higher than Z_{2p}, which means the reflected impedance Z_{eqs} in SS topology in (13) is much lower than the reflected impedance Z_{eqp} in SP topology in (7), and it means that the power received by the secondary coil in SS topology is much lower than in SP topology. It is easy to understand that the power absorbed by the reflected impedance is the power received on the secondary side.

3) $Q_L < 1$ ($Q_L < Q_{Lsf}$):

When Q_L is equal to Q_{Ls}, the η_{Link} in SS topology, as expressed in (14), attains its maximum value, denoted by

$$\eta_{\text{SS,max}} = \frac{k^2 Q_1 Q_2}{k^2 Q_1 Q_2 + 2 + 2\sqrt{1+k^2 Q_1 Q_2}}. \tag{28}$$

When $Q_L \ll 1$ ($Q_L \ll Q_{\text{Lsf}}$), the η_{Link} in SP topology [see (11)] can be simplified as

$$\begin{aligned}\eta_{\text{SP}} &\approx \frac{k^2 Q_1 Q_2^2 Q_L}{\left(1+Q_2 Q_L\right)^2 + Q_2^2 + k^2 Q_1 Q_2 \left(1+Q_2 Q_L\right)} \\ &= \frac{1}{\frac{(1+Q_2 Q_L)^2}{k^2 Q_1 Q_2^2 Q_L} + \frac{1}{k^2 Q_1 Q_L} + \frac{1+Q_2 Q_L}{Q_2 Q_L}} \\ &= \frac{1}{\frac{\left(\frac{1}{Q_2}+Q_L\right)^2+1}{k^2 Q_1 Q_L} + 1 + \frac{1}{Q_2 Q_L}}.\end{aligned} \tag{29}$$

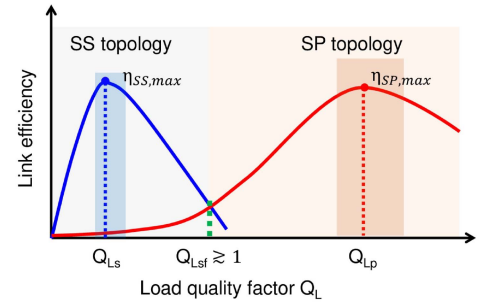

Fig. 4. Diagram illustrating link efficiency with load quality factor.

TABLE III
SELECTION BASED ON LINK EFFICIENCY

(a) Selection regarding operation frequency	
Operation frequency f	Link efficiency
$f < f_b$	SS topology <SP topology
$f = f_b$	SS topology = SP topology
$f > f_b$	SS topology >SP topology
(b) Selection regarding the secondary inductance	
$L_2 < L_{2b}$	SS topology <SP topology
$L_2 = L_{2b}$	SS topology = SP topology
$L_2 > L_{2b}$	SS topology >SP topology
(c) Selection regarding the load resistance	
$R_L < R_{Lb}$	SS topology >SP topology
$R_L = R_{Lb}$	SS topology = SP topology
$R_L > R_{Lb}$	SS topology <SP topology

Comparing (29) with (14), it is obvious that SS topology shows a better performance than SP topology, as the denominator in (29) is larger than in (14).

Link efficiency in terms of load quality factor can be depicted in Fig. 4.

C. Analyzing Boundaries

In the design of implantable devices utilizing inductive links, it is crucial to consider factors like operation frequency, load resistance, and implant size. A comprehensive summary of the choice between SS and SP topology for η_{Link}, taking into account these factors, is presented in Table III.

Given the selection factor, the secondary inductance, and the load resistance, the boundary of operation frequency is determined as

$$f_b = \frac{R_L}{2\pi L_2 Q_{\text{Lsf}}}. \tag{30}$$

When the operating frequency surpasses the boundary frequency f_b, as defined in (30), SS topology demonstrates higher η_{Link}, and conversely, vice versa. When the quality factors of both coils are significantly higher than 1, Q_{Lsf} is slightly greater than 1. The boundaries of the secondary inductance and load resistance are

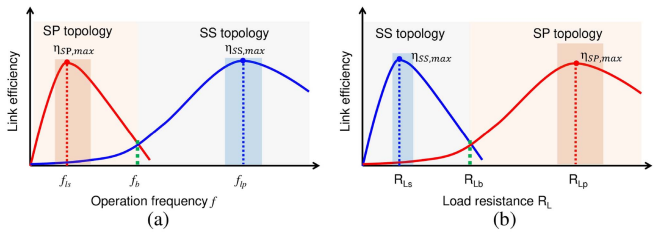

Fig. 5. Diagram illustrating link efficiency with (a) operation frequency and (b) load resistance.

determined as

$$L_{2b} = \frac{R_L}{2\pi f Q_{\mathrm{Lsf}}} \tag{31}$$

$$R_{Lb} = 2\pi f L_2 Q_{\mathrm{Lsf}}. \tag{32}$$

D. Analyzing Maximum Link Efficiency

The $\eta_{\max}$ in SS and SP topologies regarding operation frequency, secondary inductance, and load resistance are discussed.

1) *Operation frequency:*
$\eta_{\max}$ in SS topology occurs when operation frequency f equals f_{Ls}, as indicated by

$$f_{\mathrm{Ls}} = \frac{R_L}{2\pi L_2 Q_{\mathrm{Ls}}} = \frac{R_L Q_2}{2\pi L_2 \sqrt{1+k^2 Q_1 Q_2}} \tag{33}$$

and $\eta_{\max}$ in SP topology occurs at f equals f_{Lp}

$$f_{\mathrm{Lp}} = \frac{R_L}{2\pi L_2 Q_{\mathrm{Lp}}} = \frac{R_L \sqrt{1+k^2 Q_1 Q_2}}{2\pi L_2 \sqrt{1+k^2 Q_1 Q_2 + Q_2^2}}. \tag{34}$$

Based on the derivation in Section III-A, where it is shown that Q_{Ls} is less than 1 and Q_{Lp} is greater than 1, it becomes evident that f_{Lp} is lower than f_{Ls}. The link efficiency concerning operation frequency is illustrated in Fig. 5(a).

2) *Secondary inductance (L_2):*
In SS topology, $\eta_{\max}$ is achieved when L_2 equals L_{2s}

$$L_{2s} = \frac{R_L}{2\pi f Q_{\mathrm{Ls}}} = \frac{R_L Q_2}{2\pi f \sqrt{1+k^2 Q_1 Q_2}} \tag{35}$$

and $\eta_{\max}$ in SP topology occurs when L_2 equals L_{2p}

$$L_{2p} = \frac{R_L}{2\pi f Q_{\mathrm{Lp}}} = \frac{R_L \sqrt{1+k^2 Q_1 Q_2}}{2\pi f \sqrt{1+k^2 Q_1 Q_2 + Q_2^2}}. \tag{36}$$

The trend of link efficiency for the value of L_2 is the same as that depicted in Fig. 5(a), which is not presented here.

3) *Load resistance:*
The $\eta_{\max}$ in SS topology occurs when the load resistance equals R_{Ls}, as indicated by

$$R_{\mathrm{Ls}} = 2\pi f L_2 Q_{\mathrm{Ls}} = 2\pi f L_2 \sqrt{\frac{1+k^2 Q_1 Q_2}{Q_2^2}} \tag{37}$$

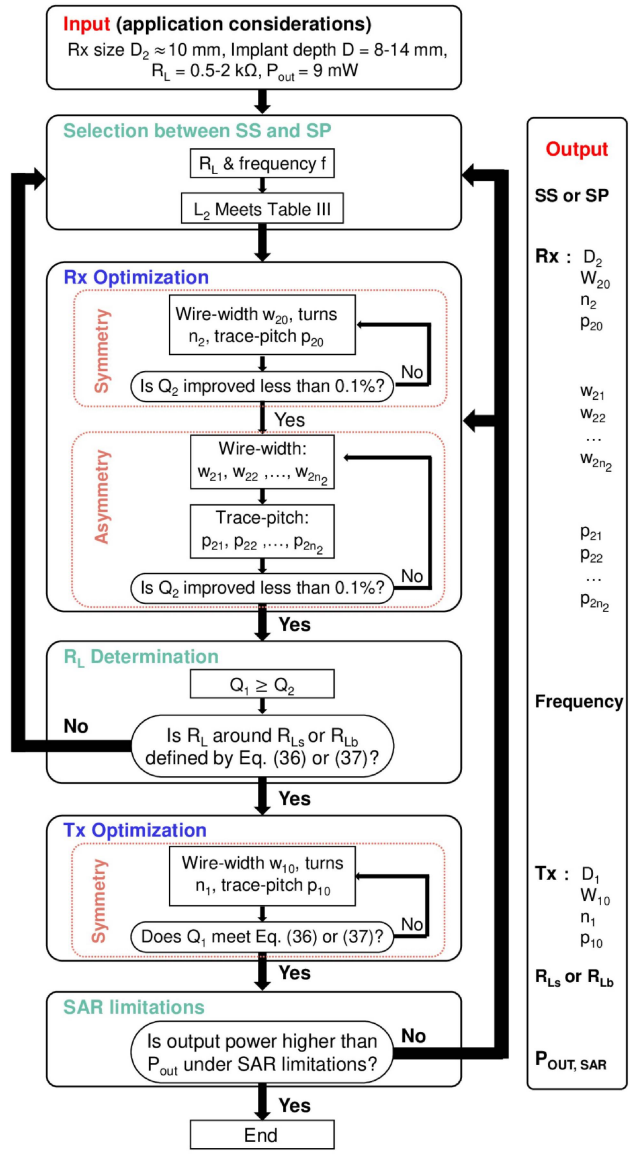

Fig. 6. Procedure for the inductive link design.

and the peak link efficiency in SP topology occurs at the R_L equals R_{Lp}, as specified

$$R_{\mathrm{Lp}} = 2\pi f L_2 Q_{\mathrm{Lp}} = 2\pi f L_2 \sqrt{1+\frac{Q_2^2}{1+k^2 Q_1 Q_2}}. \tag{38}$$

The diagram of link efficiency with load resistance is outlined in Fig. 5(b). The inductive link should be designed with a load resistance of around R_{Ls} or R_{Lp}.

E. SAR Consideration

The SAR is associated with tissue exposed to an electromagnetic field. The safety limits for a 1-g tissue, and the limit is 1.6 W/kg [36]. The value of SAR [18] can be determined using

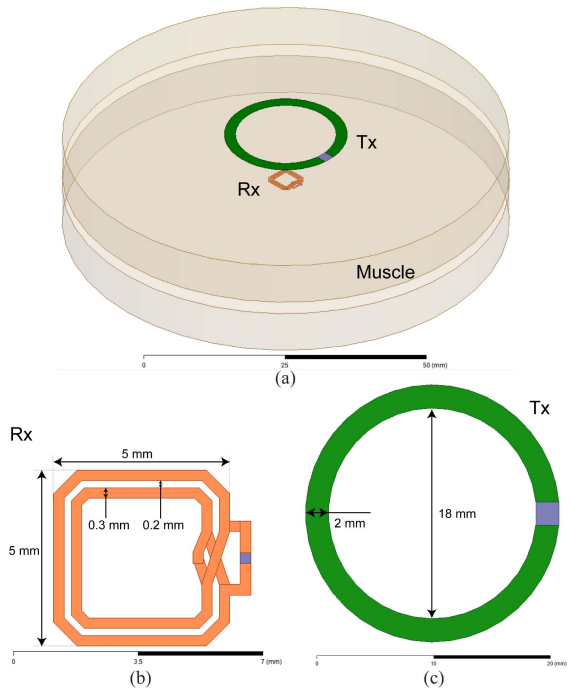

Fig. 7. (a) Inductive coupling model under an operation frequency of 400 and 300 MHz. (b) Implantable coil with two-layer structure. (c) External coil with one-layer structure.

the following equation:

$$\mathrm{SAR} = \frac{\sigma \left|E_{\mathrm{rms}}\right|^2}{\rho} \tag{39}$$

where σ denotes the conductivity of the muscle, ρ represents the density of the muscle, and E_{rms} signifies the root-mean-square value of the induced electric field. The density of the muscle tissue is 1090 kg/m^3 [36]. According to Maxwell's equations, the value of E_{rms} is proportionate to the product of the operating frequency and current ($f \times I$). Under a 1-A excitation current, the maximum SAR value is initially calculated through electromagnetic software simulation. As a result, the excitation current limit can be determined using the following equation [37]:

$$I_{1,\max} = \sqrt{\frac{1.6(\mathrm{W/kg})}{\mathrm{SAR}_{\max}}} \times 1(A). \tag{40}$$

Then, using this $I_{1,\max}$, the peak power delivered to the load can be computed in (15) and (12).

F. Guidance for Designing an Inductive Link

There are six primary steps involved in the design of an inductive link, as illustrated in Fig. 6. Begin by establishing the requirements based on applications. For an implantable hypoglossal nerve stimulator example, if Rx is placed on top of the nerve to keep it small, the outer diameter of Rx is set to be 10 mm. This considers the nerve's diameter (around 2–4 mm) and accounts for electrodes and encapsulation [38]. Given the implant's proximity to the mandible, where the skin depth is shallow, the depth is set between 8 and 14 mm. Considering the impedance of the hypoglossal NEI within a range of 0.5–2 kΩ [4], the output power of Rx is guaranteed to be at least 9 mW under a maximum stimulation current of 3 mA.

The next step is the selection between SS and SP topology based on Table II. By considering an initial frequency and R_L, the boundary of L_2 can be computed in (31), providing a framework for the subsequent Rx optimization.

The optimization of the implantable coil is based on the concept of maximizing quality factor (Q_2) as defined in (2). Three versions of the implantable coil (Rx1, Rx2, and Rx3) are considered. The optimization process for Rx1 encompasses varying wire-width (w_{20}), turns (n_2), and trace-pitch (p_{20}). Rx2 is a double-layer variant of Rx1, featuring symmetrical structures with consistent wire width for each turn and an identical trace pitch.

The self-resistance of a coil is composed of the skin-effect resistance R_{skin} and the proximity-effect resistance R_{prox} [23], as expressed by the equation

$$R_{\mathrm{total}} = R_{\mathrm{skin}} + R_{\mathrm{prox}}. \tag{41}$$

The value of R_{skin} is inversely proportional to the skin depth, which, in turn, is inversely proportional to the operating frequency f. The proximity-effect resistance R_{prox} is directly correlated with the square of the magnetic field density, which has been studied through mathematical analysis, simulation, and measurement verification [23], [25], [39]. The wire located in the innermost ring yields the highest proximity-effect resistance due to the presence of the largest magnetic field in this region. In [23], the asymmetric structure, characterized by a smaller innermost ring wire width and a larger outer ring wire width, demonstrates a quality factor enhancement of 19% compared to the conventional symmetric structure with the same width and trace-pitch. Rx3 optimization involves adjusting the wire-width and trace-pitch asymmetrically while preserving the inner radius, outer radius, and number of turns consistent with Rx2.

Subsequently, verify whether the predefined load resistance aligns with this value using (37) or (38), if Q_1 exceeds Q_2. If the load resistance significantly deviates from the specified value, return to step 2 by adjusting the operation frequency. Alternatively, if the load resistance is within an acceptable range, Tx optimization will be carried out to ensure that the quality factor Q_1 aligns with either (37) or (38). Taking advantage of the insight that Tx radius is approximately $\sqrt{2}$ times the distance between the two coils [40], the dimensions of the Tx are fine-tuned by varying the wire width, turns, and trace-pitch.

Finally, assess whether the design meets the SAR limitations. If not, revisit steps 2 or 5. If yes, output all the parameters of both Tx and Rx. An inductive link is designed following the procedure in the subsequent Section IV-B.

IV. Simulation and Measurement Results

In this section, two primary objectives are pursued.

1) Validate theoretical formulations by examining link efficiency and output power fluctuations related to load quality in SS and SP topologies. This involves investigating the

TABLE IV
DIELECTRIC PROPERTIES OF MUSCLE UNDER DIFFERENT FREQUENCIES

Name	400 MHz	300 MHz	13.56 MHz
Conductivity (S/m)	0.80	0.77	0.63
Relative permittivity	57.13	58.20	138.44
Loss tangent	0.63	0.79	6.02

selection factor to determine the boundary for operation frequency and load resistance.

2) Actively design an inductive link following the procedure to achieve $\eta_{\max}$ and measurements are conducted to evaluate the performance of this link combined with a passive rectifier and a load resistor.

The case in the first objective thoroughly analyzed an inductive link comprising an Rx coil (5 mm in diameter), a Tx coil (22 mm in diameter), and an operating frequency of 400 MHz, as depicted in Fig. 7. The choice of these particular sizes and frequency is informed by recent research, as outlined in [7], and aligns with the mid-range permissible frequencies of ISM standards [13]. In addition, a comparative analysis was performed with an operating frequency of 300 MHz.

For the secondary objective, the chosen operating frequency is 13.56 MHz. This decision stems from the findings of the first case, where operating frequencies in the hundreds of MHz resulted in the $\eta_{\max}$ at load impedances in the tens of $k\Omega$. This load impedance range is significantly higher than what is typically encountered in the classical NEI. Lowering the operating frequency can shift the load impedance to a lower value at which $\eta_{\max}$ occurs.

A. Verification of Simulations at Hundreds of MHz

Fig. 7 depicts the models of Tx and Rx, where Tx consists of a single turn on one layer with a wire width of 2 mm, and Rx comprises two turns on both layers. The separation between the coils is fixed at 10 mm. Simulations were conducted in Ansys electromagnetic software HFSS. The dielectric properties of muscle incorporated into the simulation model at 400 and 300 MHz are provided in Table IV, derived from online calculations [41]. In addition, muscle properties at 13.56 MHz are included in this table for subsequent analysis.

Table V presents the electrical parameters obtained from HFSS simulations. For Tx coil, the simulated self-inductance is 38.69 nH at an operating frequency of 300 MHz, and the simulated L_1 is 40.63 nH at 400 MHz. Notably, there is a significant disparity in parasitic resistance between the two operating frequencies, with R_1 being 1.58 Ω at 300 MHz and R_2 being 4.51 Ω at 400 MHz. The parasitic capacitance C_{s1} is determined by frequency sweeping from 100 MHz to 30 GHz to obtain the self-resonant frequency (SRF), and analyze the inductance (L_1) at the operation frequency. Finally, utilize the SRF equation $f_{s1} = 1/\sqrt{C_{s1}L_1}$ to derive C_{s1}. Typically, the operation frequency is set to be four times less than SRF [21]. Utilizing the simulated electrical parameters for both coils, the variation of η_{Link} with load quality in SS topology and SP topology is determined through (14) and (11), respectively.

TABLE V
ELECTRICAL PARAMETERS OF BOTH COILS DERIVED FROM HFSS SIMULATION

Parameters	Description	400 MHz	300 MHz
L_1 (nH)	Inductance of Tx coil	40.63	38.99
R_1 (Ω)	Resistance of Tx coil	4.51	1.58
f_{s1} (GHz)	SRF of Tx coil	1.9	1.9
C_{s1} (fF)	Capacitance of Tx coil	17.3	18
Q_1	Quality factor of Tx coil	22.63	46.13
L_2 (nH)	Inductance of Rx coil	119.71	108.81
R_2 (Ω)	Resistance of Rx coil	2.65	1.52
f_{s2} (GHz)	SRF of Rx coil	20.2	20.2
C_{s2} (fF)	Capacitance of Rx coil	0.52	0.57
Q_2	Quality factor of Rx coil	113.46	134.79
Dis (mm)	Distance between two coils	10	10
k	Coupling coefficient	$3.51e^{-2}$	$3.1e^{-2}$
n	Turns ratio	1.71	1.67
$\text{SAR}^*_{\max}$ (W/Kg)	Average SAR (simulated value)	$6.85e^2$	$4.17e^2$
Q_{Lsf}	Selection factor	1.0001	1.0002
$R_{L,\text{min, sp}}$ (Ω)	Minimum resistance selecting SP	300.7	205.0
$R_{L,\text{min, PTE}}$ ($k\Omega$)	Minimum resistance in SP with η_{Link} higher than 10%	1.4	0.52
R_{Lp} ($k\Omega$)	Resistance in SP with $\eta_{\max}$	16.72	10.46
$\text{PDL}_{\max,\text{SAR}}$ (mW)	Maximum power deliver to the load under SAR limit in SP	420.4	456.6
$\text{PDL}_{R_L=1k}$ (mW)	Power deliver to the load under SAR limit in SP with R_L of 1 $k\Omega$	46.2	61.4

$*$ Value of SAR is computed by applying a current of 1A to the Tx coil.

1) *Operation frequency (400 MHz):* Fig. 8 illustrates the simulation results obtained under an operating frequency of 400 MHz. The PTE results reveal that SS topology outperforms SP topology when the load quality factor (Q_L) is below the selection factor (Q_{Lsf}). Conversely, when Q_L exceeds Q_{Lsf}, SP topology exhibits superior performance. The value of Q_{Lsf} is nearly equal to 1, occurring when the load impedance is 300.7 Ω. Under SP topology, Q_L must exceed 4.64 to achieve a η_{Link} greater than 10%. As a result, R_L should be greater than 1.4 $k\Omega$.
SS topology shows an output power that is inversely proportional to the load quality factor, while SP topology shows an opposite trend, as illustrated in Fig. 8(b). The maximum SAR is 6.85 W/kg at 1 A, indicating that the maximum excitation current should be 0.48 A, as determined by (40). In SP topology, the maximum power delivered to the load is 7.89 mW, which is the product of the squares of 0.48 and 1.8. Note that when the load resistance is 1 $k\Omega$, the load quality is 3.32, and the power delivered to the load is only 46.2 mW under an excitation current of 0.48 A.

2) *Operation frequency (300 MHz):* In Fig. 9, simulation results obtained at 300 MHz are shown. It is noted that the η_{Link} trends in both SS and SP topologies are in agreement with those observed at 400 MHz. The value of Q_{Lsf} remains slightly higher than 1, occurring when the load impedance is 205.4 Ω. Furthermore, to achieve a η_{Link} greater than 10% under SP topology, Q_L must

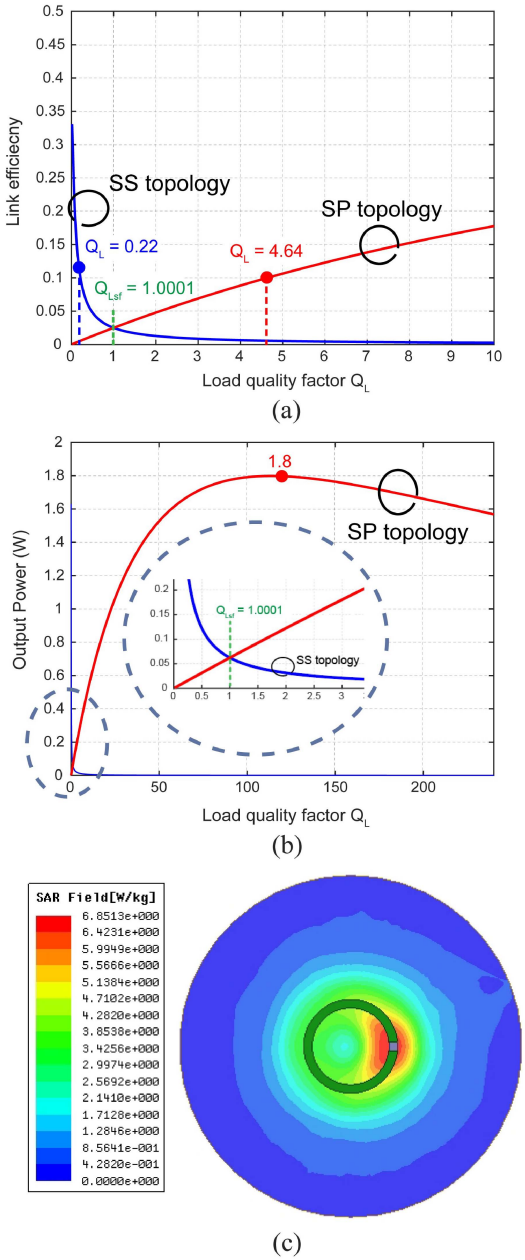

Fig. 8. Simulation results under an operating frequency of 400 MHz. (a) Variation of link efficiency with load quality. (b) Variation of output power under an excitation current of 1 A with load quality. (c) Specific absorption rate observed under an excitation current of 1 A from a top-view perspective.

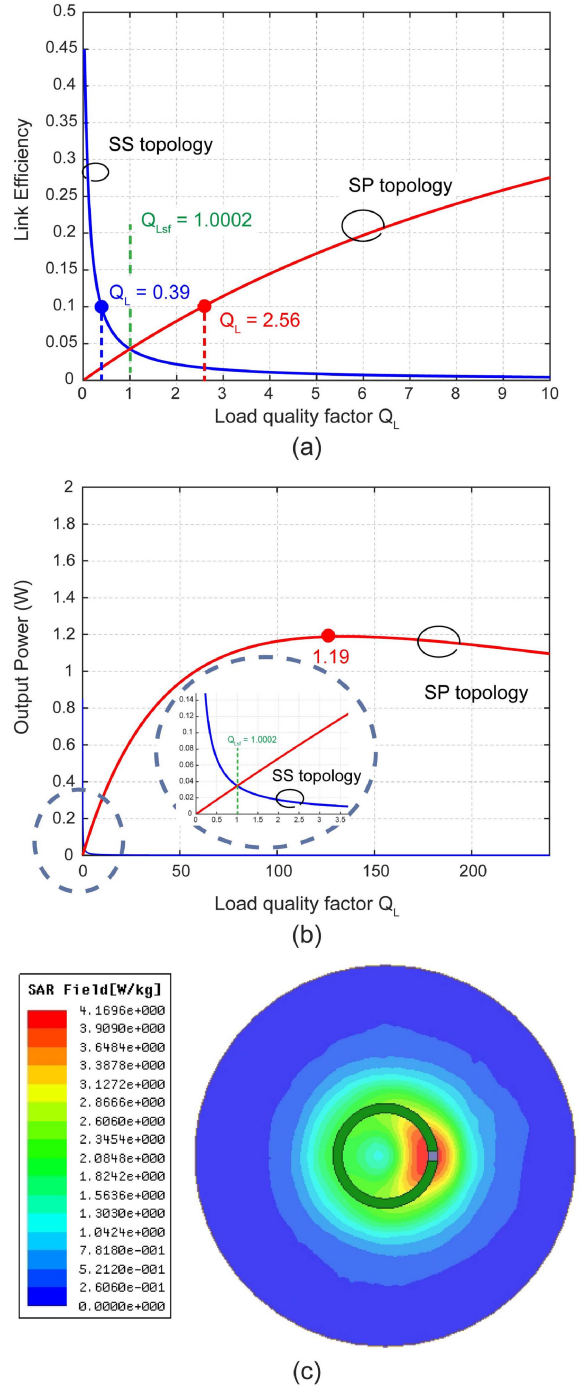

Fig. 9. Simulation results under an operating frequency of 300 MHz. (a) Variation of link efficiency with load quality. (b) Variation of output power under an excitation current of 1 A with load quality. (c) SAR observed under an excitation current of 1 A from a top-view perspective.

surpass 2.56. This implies that R_L should be greater than $0.52\,k\Omega$, which is much less than the 1.4 $k\Omega$ resistance value observed at 400 MHz.

The output power of SS topology is shown in Fig. 9(b). The maximum SAR under an excitation current of 1 A is 4.17 W/kg, which means the maximum excitation current should be 0.62 A with (40). With it and R_L of 1 $k\Omega$ ($Q_L = 2.43$), the output power is 61.39 mW.

3) *Boundary analysis Boundary of frequency:* If the R_L is less or around 300 Ω and the preference is to select SP topology, the operational frequency should be set lower than 400 MHz. The minimum resistance to select SP topology at 400 MHz is higher than at 300 MHz.

Boundary of load resistance: SS topology performs better than SP topology at 400 MHz if the load impedance is less than 300.7 Ω. If the inductive link selects SS topology at 300 MHz, the load resistance should be less than 205 Ω.

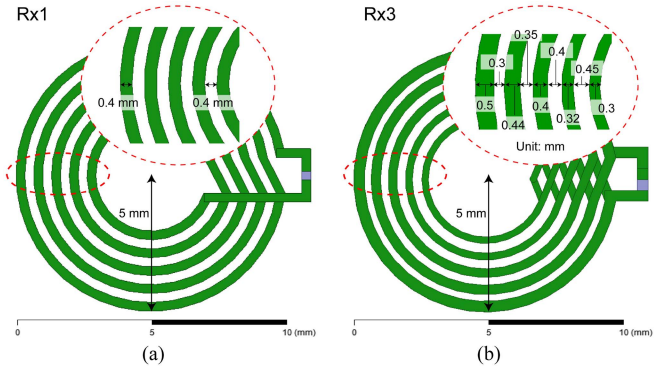

Fig. 10. Implantable coil at 13.56 MHz. (a) Rx1 is a single-layer design with a uniform wire width. (b) Rx3 is a two-layer design with asymmetric wire widths. Note: Rx2 is a two-layer design based on Rx1.

It is worth noting that with $\eta_{\max}$ occurring, the load resistance is 16.72 $k\Omega$ at 400 MHz and 10.46 $k\Omega$ at 300 MHz), significantly surpassing the value of classical NEI. In addition, the load resistance needed to achieve $\eta_{\max}$ at 300 MHz is 10.46 $k\Omega$, which is lower than the value of 16.72 $k\Omega$ at 400 MHz. This indicates that opting for an operating frequency significantly lower than 300 MHz is preferable to attain $\eta_{\max}$, occurring at a load resistance of approximately 1 $k\Omega$.

Note that the measurement results for this inductive link at 400 and 300 MHz are not presented here, as previous research in [7] and [19] has shown that the measurement results match well with simulation results using the de-embedding calibration technique.

B. Application Design at 13.56 MHz

A pair of coils is designed following the procedure outlined in Section III-F. Fig. 10 illustrates the geometry of Rx. The simulated electrical parameters of Rx, the coupling factor between Tx and Rx, as well as the measured results, are presented in Fig. 11. Notably, L_2 in Rx3 (measured 1.15 μH, simulated 0.9 μH) surpasses that of Rx2 and is significantly greater than Rx1 in both simulated and measured results. Regarding resistance, R_2 in Rx3 (measured 1.46 Ω, simulated 0.98 Ω) is slightly smaller than Rx2 but higher than Rx1. The enhanced Rx3 exhibits the highest quality factor value.

The final geometry of Tx is shown in Fig. 12(a) and the outer radius is 14.5 mm with eight turns. The simulated inductance, parasitic impedance, and quality factor are compared with the measured results, as is shown In Fig. 12(b), we can see that the simulated L_1 (2.03 μH) is almost the same with the measured result (2.01 μH), and the measured R_1 is 1.5 Ω which is larger than the simulated 1.23 Ω, resulting the measured Q_1 of 114.1 is smaller than the simulated 140.5. Fig. 12(c) presents the SAR under 1 A excitation current with the maximum value of 2.79 W/kg. Based on (40), the maximum excitation current should be 0.76 A with the SAR limit. The simulated coupling factor remains nearly identical in the three versions of Rx (0.08),

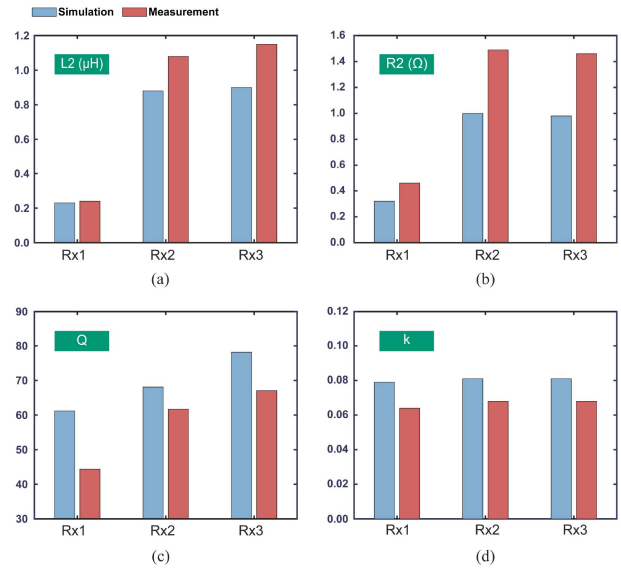

Fig. 11. Implantable coil Parameters derived from HFSS simulation and measurement in three versions (Rx1, Rx2, Rx3). (a) Self-inductance. (b) Parasitic resistance. (c) Quality factor. (d) Coupling coefficient between external coil and implantable coil.

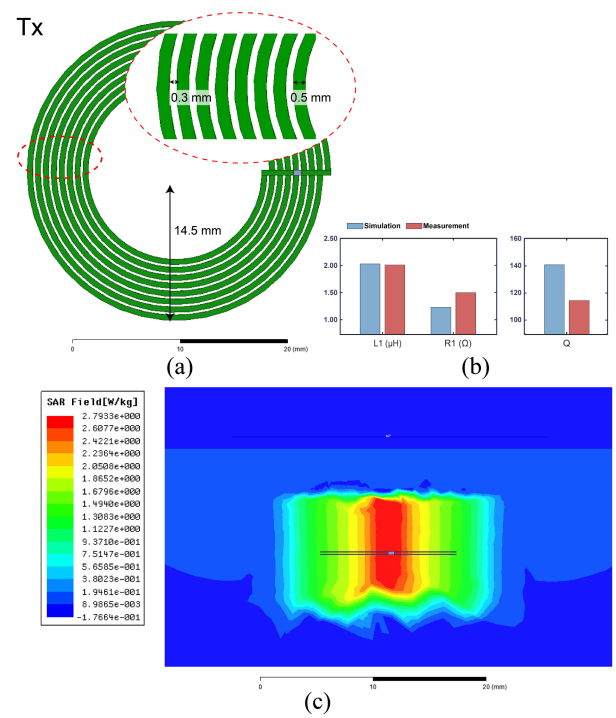

Fig. 12. (a) External coil under an operation frequency of 13.56 MHz. (b) Parameters derived from HFSS simulation and measurement. (c) SAR observed from a lateral view under an excitation current of 1 A.

slightly exceeding the measured value (0.065), as is shown in Fig. 11(d).

The measurement setup for the inductive link, featuring a passive rectifier and load, is depicted in Fig. 13, with labeled instruments. The GWINSTEK arbitrary function generator AFG3032 serves as an external power source denoted by ①. The Keysight

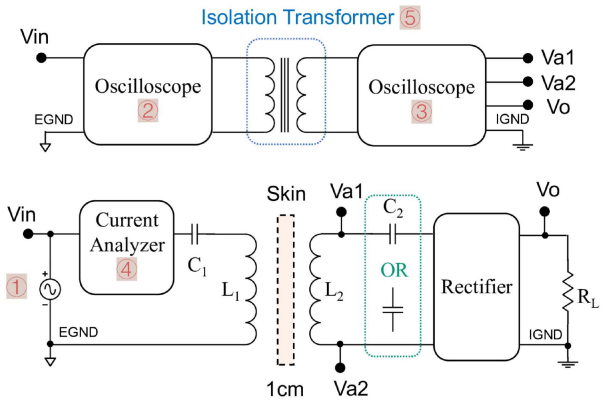

Fig. 13. Measurement setup for SS or SP topology with a passive rectifier and load impedance.

DSOX3034 T and Keysight MSOS604 A oscilloscopes, denoted by ② and ③, respectively, are tasked with monitoring the external voltage and internal voltage, respectively. External current analysis is performed by the Keysight CX3324 A, indicated by ④. Note that the ground in the external coil differs from that in the implantable coil, an isolation transformer marked ⑤ is used to connect them. To obtain η_{Link}, the overall efficiency of the setup is calculated and then divided by the power conversion efficiency of the rectifier. Fig. 14 presents the results of η_{Link} and the output power variation with load quality for three versions of the implantable coil. The power delivered to the load is measured under an excitation current of 0.1 A, a value significantly below the maximum excitation current requirement of 0.85 A imposed by SAR limits. Compensated capacitors, C_1 and C_2, are incorporated to achieve resonance with inductors L_1 and L_2 at 13.56 MHz. Specifically, C_1 is chosen as 68 pF, and C_2 in the Rx3 structure is set to 120 pF. In this experiment, beef was employed as a substitute to mimic muscle tissue. The depth of the implantable coil was set to 10 mm on a position stage, which was manually controlled by a rotating handle.

The results depicted in Fig. 14 indicate that SP topology exhibits significantly higher η_{Link} compared to SS topology across all three versions of the receiver coil (Rx). The load resistance varies from 200 Ω to 2 $k\Omega$, and the load quality is determined based on (2), incorporating the measured self-inductance from Fig. 11.

In Fig. 14(a), when R_L is set at 200 Ω and a measured L_2 value of 0.23 μH, the resulting Q_L is 10.2, significantly exceeding the selection factor. Rx1 exhibits higher η_{Link} than Rx2 and Rx3 when R_L is less than 400 Ω. However, with the increase in Q_L, the η_{Link} of Rx1 experiences a significant decline. With Rx3, when R_L equals 1 $k\Omega$ ($Q_L = 10.2$), the η_{Link} reaches 71.45%, surpassing the η_{Link} of Rx2 at 70.4%, and significantly outperforming Rx1, which records a η_{Link} of 43.6%. This indicates that Rx3 improves efficiency by 27.85% compared to Rx1. Specifically, the highest η for Rx3 is reached when R_L is 0.92 $k\Omega$ in the simulation result and 1.12 $k\Omega$ in the measurement result, which meets the design objective of $\eta_{\max}$ occurring at R_L of around 1 $k\Omega$.

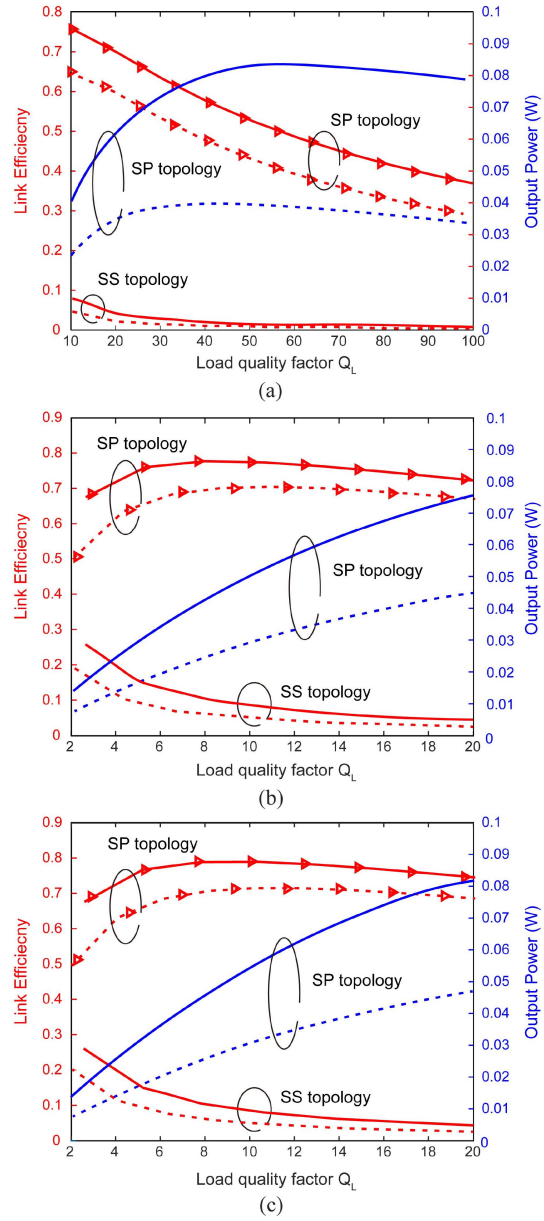

Fig. 14. Plotting of load quality factor with link efficiency (*Y*-axis on the left-hand side colored in red), and output power (*Y*-axis on the right-hand side colored in blue). Solid lines and dotted lines represent simulated and measured results, respectively. Different versions of receiver coils. (a) Rx1. (b) Rx2. (c) Rx3.

Under an excitation current I_1 of 0.1 A, Rx1 achieves the maximum power delivery to the load ($\text{PDL}_{\max}$) at 39.2 mW with Q_L equal to 40.8 ($R_L = 800$ Ω). In contrast, Rx3 demonstrates a PDL of 47.6 mW when Q_L is 20 ($R_L = 1.96\ k\Omega$). Significantly, Rx3 achieves the $\text{PDL}_{\max}$ of 3.83 W, adhering to the SAR limit's maximum excitation current requirement of 0.76 A, corresponding to a Q_L value of 59.2.

The simulated η_{Link} and coupling coefficient concerning Rx3's misalignment in the *X*-direction and displacement in implant depth (*Z*-direction) are illustrated in Fig. 15(a) and (b), respectively. With an increase in misalignment and displacement, there is a reduction in both coupling coefficient and η_{Link}. For

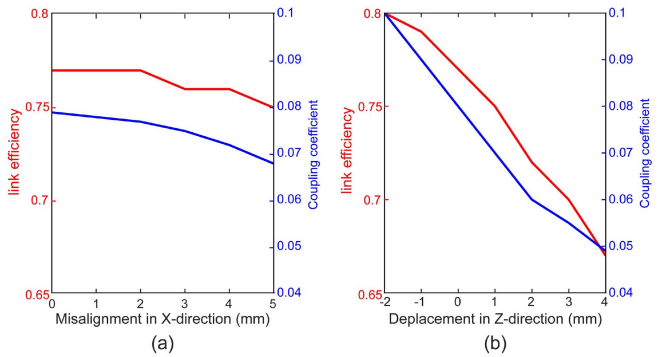

Fig. 15. Simulated values of link efficiency and coupling coefficient plotted against Rx's (a) misalignment in the *X*-direction and (b) displacement in implant depth (*Z*-direction).

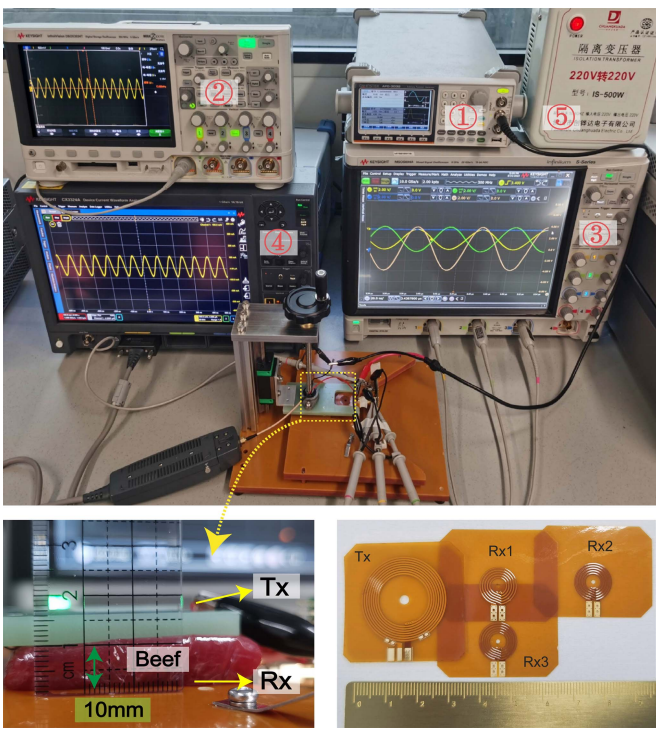

Fig. 16. Photograph of measurement setup for SP topology with a passive rectifier and load.

misalignment in the *X*-direction ranging from 0 to 5 mm, η_{Link} exhibits a decrease from 0.78 to 0.75. In the case of displacement in the *Z*-direction spanning from -2 to 4 mm, η_{Link} decreases from 0.8 to 0.67. Remarkably, the effect of displacement in the *Z*-direction on η_{Link} is more significant than that in the *X*-direction.

In corresponding to the setup depicted in Fig. 13. Fig. 16 provides a photograph showcasing the same instruments with marked labels. The peak-to-peak value of the excitation voltage is 1.11 V, and the amplitude of the external current is 0.1 A. Under R_L of 500 Ω, the measured voltage across the load is 3.61 V, with a peak-to-peak value between the implantable coil reaching 3.92 V, as is shown in Fig. 17. The total efficiency

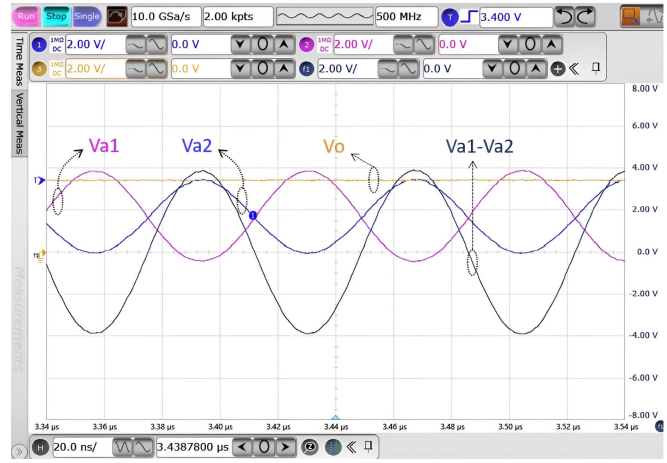

Fig. 17. Measurement voltages across the internal coil and the output voltage of the rectifier.

TABLE VI
COMPARISON OF INDUCTIVE LINK FOR IMPLANTABLE DEVICE (IMD) AT SEVERAL MHZ

Parameters		[4]	[42]	[43]	[44]	This work (Mea.)
Tx	D_1 (mm)	35	30	24	52	29
	n_1	9	N/A	2	7	8
Rx	D_2 (mm)	9.2	22	10	10	10
	n_2	4	N/A	7	5	5
	l_2	1	1	1	1	2
D (mm)		5	N/A	10	20	10
Freq. (MHz)		2	13.56	13.56	25	13.56
$\eta_{\text{link, air}}$ (%)		39.8	76.3	N/A	44.1	72.5
$\eta_{\text{link, tissue}}$ (%)		31.8	N/A	30.84	N/A	62.99
$R_L(k\Omega)$		N/A	N/A	0.5	1	0.5
$\text{PDL}_{\max}$ (mW)		20	N/A	N/A	145.4	3.83 e^3
SAR (W/kg)		1.6	N/A	N/A	2	1.6

D_1: Outer diameter of Tx. n_1: Number of turns of Tx.
D_2: Outer diameter of Rx. n_2: Number of turns of Rx.
l_2: Number of layers of Rx. D: Implant depth.

is calculated at 46.96%, comprising a η_{Link} of 62.99% and a rectifier efficiency of 74.14%.

Table VI illustrates a comparison of an inductive link aimed at implant applications with comparable outer diameters of Rx and frequencies in the MHz range. The measured η_{Link} under beef tissue is 62.99% at R_L of 0.5 $k\Omega$, which is much higher than the value of 30.84% with the same operation frequency and same outer diameter of Rx provided in [43]. Specifically, in [42], the η_{Link} between two coils under an air medium is 76.3%, higher than our measured results of 72.5% due to the size of the Rx size being two times larger than ours. In terms of muscle variations, there is no significant influence on the mutual coupling coefficient, but they do impact the quality factor, as evidenced by studies in [19], [21], and [43]. To investigate this further, simulations were conducted to analyze the inductive link under both air gap and muscle conditions. The results suggest that while the coupling coefficient remains relatively unchanged,

there is a slight increase in the quality factor. Consequently, the link efficiency experiences a marginal increase of less than 1%.

V. Conclusion

In this work, formula expressions for link efficiency and output power are derived utilizing quality factors with reflected impedance model. Based on these expressions, the selection between SS and SP topologies, and maximum link efficiency are comprehensively analyzed with operation frequency, self-inductance, and load impedance. In addition, an inductive link design procedure aimed at achieving $\eta_{\max}$ in inductive links is proposed. Besides, an asymmetric coil is designed to achieve a higher quality factor and enhance link efficiency in comparison to the conventional symmetric coil. The analysis is verified through simulation and measurement, along with SAR consideration. These contributions significantly advance WPT systems for biomedical applications, emphasizing efficiency enhancements and adherence to safety standards.

Acknowledgment

The authors would like to thank Qiming Hou and Di Wu from Westlake University for their technical support.

References

[1] W. Zhang, S.-C. Wong, K. T. Chi, and Q. Chen, "Design for efficiency optimization and voltage controllability of series–series compensated inductive power transfer systems," *IEEE Trans. Power Electron.*, vol. 29, no. 1, pp. 191–200, Jan. 2014.

[2] C. Vivarelli et al., "Electromagnetic immunity of pacemakers and implantable defibrillators to wireless power transfer systems for automotive: A provocative study," *IEEE Trans. Electromagn. Compat.*, vol. 66, no. 1, pp. 97–107, Feb. 2024.

[3] G. L. Barbruni, F. Rodino, P. M. Ros, D. Demarchi, D. Ghezzi, and S. Carrara, "A wearable real-time system for simultaneous wireless power and data transmission to cortical visual prosthesis," *IEEE Trans. Biomed. Circuits Syst.*, vol. 18, no. 3, pp. 580–591, 2024.

[4] F. Xia et al., "Minimally invasive hypoglossal nerve stimulator enabled by ECG sensor and WPT to manage obstructive sleep apnea," *Sensors*, vol. 23, no. 21, 2023, Art. no. 8882.

[5] Z. Xue, S. Fan, D. Li, L. Zhang, W. Gou, and L. Geng, "A 13.56MHz, 94.1% peak efficiency CMOS active rectifier with adaptive delay time control for wireless power transmission systems," *IEEE J. Solid-State Circuits*, vol. 54, no. 6, pp. 1744–1754, Jun. 2019.

[6] J. Lee et al., "Neural recording and stimulation using wireless networks of microimplants," *Nature Electron.*, vol. 4, no. 8, pp. 604–614, 2021.

[7] Y. Zhang et al., "An 8-shaped antenna-based battery-free neural-recording system featuring 3cm reading range and 140 pJ/bit energy efficiency," *IEEE J. Solid-State Circuits*, vol. 53, no. 11, pp. 3194–3206, Nov. 2023.

[8] A. Trigui, S. Hached, F. Mounaim, A. C. Ammari, and M. Sawan, "Inductive power transfer system with self-calibrated primary resonant frequency," *IEEE Trans. Power Electron.*, vol. 30, no. 11, pp. 6078–6087, Nov. 2015.

[9] F. Mao, Y. Lu, and R. P. Martins, "A reconfigurable cross-connected wireless-power transceiver for bidirectional device-to-device wireless charging," *IEEE J. Solid-State Circuits*, vol. 54, no. 9, pp. 2579–2589, Sep. 2019.

[10] Z. Sun, Y. Wang, M. Li, Y. Guan, and D. Xu, "Analysis and design of 6.78M WPT architecture for configurable power applications based on DCX energy synthesis and functional execution," *IEEE Trans. Power Electron.*, vol. 39, no. 1, pp. 106–111, Jan. 2024.

[11] H. Kim, Y. Park, and C. Kim, "A 13.56-MHz wireless power transfer system with a wide operating distance and load range for biometric smartcards," *IEEE Trans. Power Electron.*, vol. 38, no. 4, pp. 5576–5585, Apr. 2023.

[12] X. Yang, Y. Li, W. Sun, J. Chen, Y. Peng, and Z. He, "A simultaneous power and data transfer technology using dual-resonance-band circuits for domino-resonator WPT systems," *IEEE Trans. Ind. Inform.*, vol. 20, no. 1, pp. 269–279, Jan. 2024.

[13] V. Shevchenko, O. Husev, R. Strzelecki, B. Pakhaliuk, N. Poliakov, and N. Strzelecka, "Compensation topologies in IPT systems: Standards, requirements, classification, analysis, comparison and application," *IEEE Access*, vol. 7, pp. 120559–120580, 2019.

[14] R. Jegadeesan and Y.-X. Guo, "Topology selection and efficiency improvement of inductive power links," *IEEE Trans. Antennas Propag.*, vol. 60, no. 10, pp. 4846–4854, Oct. 2012.

[15] M. Ishihara, K. Umetani, and E. Hiraki, "Strategy of topology selection based on quasi-duality between series–series and series–parallel topologies of resonant inductive coupling wireless power transfer systems," *IEEE Trans. Power Electron.*, vol. 35, no. 7, pp. 6785–6798, Jul. 2019.

[16] K. Van Schuylenbergh and R. Puers, *Inductive Powering: Basic Theory and Application to Biomedical Systems*. Berlin, Germany: Springer, 2009.

[17] Y. Lu and W.-H. Ki, *CMOS Integrated Circuit Design for Wireless Power Transfer*. Berlin, Germany: Springer, 2018.

[18] A. Ibrahim and M. Kiani, "A figure-of-merit for design and optimization of inductive power transmission links for millimeter-sized biomedical implants," *IEEE Trans. Biomed. Circuits Syst.*, vol. 10, no. 6, pp. 1100–1111, Dec. 2016.

[19] D. Ahn and M. Ghovanloo, "Optimal design of wireless power transmission links for millimeter-sized biomedical implants," *IEEE Trans. Biomed. Circuits Syst.*, vol. 10, no. 1, pp. 125–137, Feb. 2016.

[20] S. Mehri, A. C. Ammari, J. B. H. Slama, and M. Sawan, "Design optimization of multiple-layer PSCs with minimal losses for efficient and robust inductive wireless power transfer," *IEEE Access*, vol. 6, pp. 31924–31934, 2018.

[21] S. A. Mirbozorgi, P. Yeon, and M. Ghovanloo, "Robust wireless power transmission to mm-sized free-floating distributed implants," *IEEE Trans. Biomed. Circuits Syst.*, vol. 11, no. 3, pp. 692–702, Jun. 2017.

[22] P. Yeon, S. A. Mirbozorgi, J. Lim, and M. Ghovanloo, "Feasibility study on active back telemetry and power transmission through an inductive link for millimeter-sized biomedical implants," *IEEE Trans. Biomed. Circuits Syst.*, vol. 11, no. 6, pp. 1366–1376, Dec. 2017.

[23] C. M. Awuah, P. Danuor, J.-I. Moon, and Y.-B. Jung, "Novel coil design and analysis for high-power wireless power transfer with enhanced Q-factor," *Sci. Rep.*, vol. 13, no. 1, 2023, Art. no. 4187.

[24] S. R. Cove, M. Ordonez, N. Shafiei, and J. Zhu, "Improving wireless power transfer efficiency using hollow windings with track-width-ratio," *IEEE Trans. Power Electron.*, vol. 31, no. 9, pp. 6524–6533, Sep. 2016.

[25] T.-H. Kim, G.-H. Yun, W. Y. Lee, and J.-G. Yook, "Asymmetric coil structures for highly efficient wireless power transfer systems," *IEEE Trans. Microw. Theory Techn.*, vol. 66, no. 7, pp. 3443–3451, Jul. 2018.

[26] W. Zhong and S. Hui, "Maximum energy efficiency tracking for wireless power transfer systems," *IEEE Trans. Power Electron.*, vol. 30, no. 7, pp. 4025–4034, Jul. 2015.

[27] H. Li, J. Li, K. Wang, W. Chen, and X. Yang, "A maximum efficiency point tracking control scheme for wireless power transfer systems using magnetic resonant coupling," *IEEE Trans. Power Electron.*, vol. 30, no. 7, pp. 3998–4008, Jul. 2015.

[28] D.-W. Seo, J.-H. Lee, and H.-S. Lee, "Optimal coupling to achieve maximum output power in a WPT system," *IEEE Trans. Power Electron.*, vol. 31, no. 6, pp. 3994–3998, Jun. 2016.

[29] S.-H. Wang et al., "Design of a bone-guided cochlear implant microsystem with monopolar biphasic multiple stimulations and evoked compound action potential acquisition and its in vivo verification," *IEEE J. Solid-State Circuits*, vol. 56, no. 10, pp. 3062–3076, Oct. 2021.

[30] Q. Chen, S. C. Wong, K. T. Chi, and X. Ruan, "Analysis, design, and control of a transcutaneous power regulator for artificial hearts," *IEEE Trans. Biomed. Circuits Syst.*, vol. 3, no. 1, pp. 23–31, Feb. 2009.

[31] C.-S. Wang, G. A. Covic, and O. H. Stielau, "Power transfer capability and bifurcation phenomena of loosely coupled inductive power transfer systems," *IEEE Trans. Ind. Electron.*, vol. 51, no. 1, pp. 148–157, Feb. 2004.

[32] Y. Chen et al., "Nonlinear modeling and harmonic analysis of magnetic resonant WPT system based on equivalent small parameter method," *IEEE Trans. Ind. Electron.*, vol. 66, no. 8, pp. 6604–6612, Aug. 2019.

[33] Y. Fang and B. M. H. Pong, "Multiple harmonics analysis for variable frequency asymmetrical pulsewidth-modulated wireless power transfer systems," *IEEE Trans. Ind. Electron.*, vol. 66, no. 5, pp. 4023–4030, May 2019.

[34] J. Hu, J. Zhao, and C. Cui, "A wide charging range wireless power transfer control system with harmonic current to estimate the coupling coefficient," *IEEE Trans. Power Electron.*, vol. 36, no. 5, pp. 5082–5094, May 2021.
[35] D. W. Hart and D. W. Hart, *Power Electronics*. New York, NY, USA: McGraw-Hill, 2011.
[36] G. Sun, B. Muneer, Y. Li, and Q. Zhu, "Ultracompact implantable design with integrated wireless power transfer and RF transmission capabilities," *IEEE Trans. Biomed. Circuits Syst.*, vol. 12, no. 2, pp. 281–291, Apr. 2018.
[37] A. Christ, M. Douglas, J. Nadakuduti, and N. Kuster, "Assessing human exposure to electromagnetic fields from wireless power transmission systems," *Proc. IEEE*, vol. 101, no. 6, pp. 1482–1493, Jun. 2013.
[38] F. Xia and M. Sawan, "Electrode-nerve interface properties to treat patients with OSA through electrical stimulation," in *Proc. IEEE 6th Int. Conf. Adv. Biomed. Eng.*, 2021, pp. 121–124.
[39] I. Lope, C. Carretero, J. Acero, R. Alonso, and J. M. Burdío, "AC power losses model for planar windings with rectangular cross-sectional conductors," *IEEE Trans. Power Electron.*, vol. 29, no. 1, pp. 23–28, Jan. 2014.
[40] T. Sun, X. Xie, and Z. Wang, *Wireless Power Transfer for Medical Microsystems*. Berlin, Germany: Springer, 2013.
[41] D. Andreuccetti, "An Internet resource for the calculation of the dielectric properties of body tissues in the frequency range 10 Hz-100GHz," 2012. [Online]. Available: http://niremf.ifac.cnr.it/tissprop/
[42] C.-Y. Wu, X.-H. Qian, M.-S. Cheng, Y.-A. Liang, and W.-M. Chen, "A 13.56MHz 40mW CMOS high-efficiency inductive link power supply utilizing on-chip delay-compensated voltage doubler rectifier and multiple LDOs for implantable medical devices," *IEEE J. Solid-State Circuits*, vol. 49, no. 11, pp. 2397–2407, Nov. 2014.
[43] U.-M. Jow and M. Ghovanloo, "Modeling and optimization of printed spiral coils in air, saline, and muscle tissue environments," *IEEE Trans. Biomed. Circuits Syst.*, vol. 3, no. 5, pp. 339–347, Oct. 2009.
[44] J. Bao, S. Hu, Z. Xie, G. Hu, Y. Lu, and L. Zheng, "Optimization of the coupling coefficient of the inductive link for wireless power transfer to biomedical implants," *Int. J. Antennas Propag.*, vol. 2022, pp. 1–12, 2022.

Fen Xia (Student Member, IEEE) received the master's degree in electromagnetic field and microwave technology from South China University of Technology, Guangzhou, China, in 2013. She is currently working toward the Ph.D. degree in research on wireless neurostimulation system with minimal invasiveness for apnea management with Zhejiang University, Hangzhou, China.

From 2013 to 2014, she was a Teaching Lecturer with XiangNan University, Chenzhou, China. In 2014, she joined the Department of Electronics and Electrical Engineering, Southern University of Science and Technology as a Research Engineer. She is currently with the Center of Excellence in Biomedical Research on Advanced Integrated-on-chip Neurotechnologies (CenBRAIN Neurotech), Westlake University, Hangzhou, China.

Fangyu Mao (Member, IEEE) received the B.S. and M.E. degrees in microelectronics from the University of Electronic Science and Technology of China (UESTC), Chengdu, China, in 2012 and 2015, respectively, and the Ph.D. degree in electrical and computer engineering from the University of Macau, Macao, China, in 2020.

In 2020, he joined the Stated Key Laboratory of Analog and Mixed-Signal VLSI, University of Macau, as a Postdoctoral Fellow, where he became a Research Assistant Professor in 2022. In 2023, he joined Light Semibucks Company, Ltd., as CTO. His research interests include wireless power transfer, power management ICs, and HV drivers.

Yan Lu (Senior Member, IEEE) received the Ph.D. degree in electronic and computer engineering from The Hong Kong University of Science and Technology (HKUST), Hong Kong, in 2013.

In 2014, he joined the State Key Laboratory of Analog and Mixed-Signal VLSI, University of Macau, Macau, China, where he is currently an Associate Professor. He has authored or coauthored more than 160 peer-reviewed technical articles and two books. His research interests include high-density power converters, integrated voltage regulators, wireless power transfer, and energy-harvesting circuits and systems.

Dr. Lu has was an ITPC Member (2020–2024) for ISSCC, as a TPC Member (2019–2022) and then the Power Management Subcommittee Chair (2023–2024) for CICC, and an IEEE SSCS Distinguished Lecturer (2022–2023). He was a Guest Editor for the IEEE JOURNAL OF SOLID-STATE CIRCUITSin 2022 and 2023, IEEE TRANSACTIONS ON CIRCUITS AND SYSTEMS I: REGULAR PAPERS in 2019, and IEEE TRANSACTIONS ON CIRCUITS AND SYSTEMS II: EXPRESS BRIEFS in 2018 and 2019. He was also a Young Editor (2021–2023) and has been an Associate Editor (Direction-2: IC Design and Applications) for the *Journal of Semiconductors* since 2024. He was the recipient or corecipient of the IEEE Solid-State Circuits Society Pre-Doctoral Achievement Award (2013–2014), the IEEE CAS Society Outstanding Young Author Award in 2017, and the ISSCC 2017 Takuo Sugano Award for Outstanding Far-East Paper.

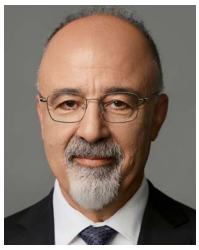

Mohamad Sawan (Life Fellow, IEEE) received the Ph.D. degree in computerized transcutaneous control of a multichannel implantable urinary prosthesis from the University of Sherbrooke, Sherbrooke, QC, Canada, in 1990.

He is currently a Chair Professor with Westlake University, Hangzhou, China, and Emeritus Professor with Polytechnique Montreal, Montreal, QC, Canada. He is the Founder and Director of the Center of Excellence in Biomedical Research on Advanced Integrated-on-chip Neurotechnologies (CenBRAIN Neurotech), Westlake University, and of the Polystim Neurotech Lab, Polytechnique Montreal. He has authored or coauthored more than 1000 peer-reviewed papers, one handbook, three books, 13 book chapters, 15 patents, and 25 other patents are pending.

Dr. Sawan was a Distinguished Lecturer of both CASS and SSCS for three consecutive years each. He was a Co-Founder, an Associate Editor, and the Editor-in-Chief of IEEE TRANSACTIONS ON BIOMEDICAL CIRCUITS AND SYSTEMS (2016–2019). He was the recipient of the Canada Research Chair in Smart Medical Devices (2001–2015), the Barbara Turnbull Award from the Canadian Institutes of Health Research (CIHR), the J.A. Bombardier and Jacques-Rousseau Awards from the Canadian ACFAS, the Queen Elizabeth II Golden Jubilee Medal, the Medal of Merit from the President of Lebanon, the Shanghai International Collaboration Award, the Chinese Government Friendship Award, the Hangzhou Outstanding Talent Award, and the Chinese Zhejiang Westlake Friendship Award. He was leading the Microsystems Strategic Alliance of Quebec (ReSMiQ), Canada (1999–2018). He is a Fellow of the Royal Society of Sciences of Canada (FRSC), Canadian Academy of Engineering (FCAE), and Engineering Institutes of Canada (FEIC), and an "Officer" of the National Order of Quebec.